Processing and Application of Ceramics 19 [4] (2025) 389–395
https://doi.org/10.2298/PAC2504389W

Electrical properties of entropy-stabilized $Li_{0.25}La_{0.25}NbO_3$ solid electrolyte ceramics

Yuxin Wang, Weiwei Hu*, Yazhou Kong*, Jie Chang, Zimeng Shi, Guang Hu, Kailong Zhang

National & Local Joint Engineering Research Center for Mineral Salt Deep Utilization, Faculty of Chemical Engineering, Huaiyin Institute of Technology, Huaian 223003, P.R. China

Received 23 October 2025; Received in revised form 4 December 2025; Accepted 11 December 2025

Abstract

Oxide all-solid-state lithium batteries (ASSLBs) are promising candidates for next-generation energy storage due to their high energy density and enhanced safety. However, their commercial application is still hindered by the relatively low conductivity of solid electrolytes. To address this issue, a high-entropy strategy was employed to improve the conductivity of $Li_{0.25}La_{0.25}NbO_3$ (LLNO). A series of entropy-stabilized solid electrolyte ceramics was synthesized via a conventional solid-state reaction method by co-doping five distinct cations (Ta^{5+}, Hf^{4+}, Zr^{4+}, Ti^{4+}, W^{6+}) at the B-site of LLNO. XRD and SEM characterizations confirmed the formation of a perovskite structure in all synthesized samples, including the pristine LLNO, $Li_{0.25}La_{0.25}Nb_{0.9}(Ta_{0.02}Hf_{0.02}Zr_{0.02}Ti_{0.02}W_{0.02})O_3$ (LLNO-1), $Li_{0.25}La_{0.25}Nb_{0.8}(Ta_{0.04}Hf_{0.04}Zr_{0.04}Ti_{0.04}W_{0.04})O_3$ (LLNO-2) and $Li_{0.25}La_{0.25}Nb_{0.7}(Ta_{0.06}Hf_{0.06}Zr_{0.06}Ti_{0.06}W_{0.06})O_3$ (LLNO-3). AC-impedance and DC-polarization measurements demonstrated that the optimized composition of the sample LLNO-2 exhibited a conductivity of 4.68×10^{-6} S/cm and electronic conductivity of 5.30×10^{-8} S/cm with a low activation energy of 0.206 eV, representing a fourfold improvement over the pristine LLNO (conductivity 1.17×10^{-6} S/cm). Although the LLNO-3 ceramics showed the highest conductivity of 6.44×10^{-6} S/cm, it was associated with high activation energy of 0.218 eV and electronic conductivity of 1.28×10^{-7} S/cm. This work demonstrates that high-entropy strategy is a promising for enhancing the conductivity of perovskite-type solid electrolytes for ASSLBs.

Keywords: *high-entropy ceramics, $Li_{0.25}La_{0.25}NbO_3$, lithium batteries, conductivity, solid electrolyte*

I. Introduction

Driven by the rapidly growing global demand for renewable energy and electric vehicles, the development of electrochemical energy storage systems that combine high safety and high energy density has become a central focus of both scientific research and industrial applications. All-solid-state lithium batteries (ASSLBs), which utilize non-flammable solid electrolytes, hold the promise of fundamentally addressing the safety hazards associated with conventional liquid lithium-ion batteries, such as electrolyte leakage, combustion and explosion. Furthermore, ASSLBs offer the potential for higher energy density and longer life cycle, making them widely regarded as a leading candidate for the next generation energy storage technology [1,2]. Within this architecture, the solid electrolyte (a key component responsible for conducting lithium ions and separating the cathode and anode) plays a decisive role in determining the overall battery performance [3].

Among various solid electrolyte materials, oxide electrolytes have garnered significant attention due to their excellent chemical stability, wide electrochemical window and favourable mechanical strength [4]. Among them, perovskite-type oxide electrolytes (general formula ABO_3) represent an important research focus, owing to their highly tunable structure and well-defined lithium-ion migration pathways [5]. $Li_{0.34}La_{0.51}TiO_{2.94}$ (LLTO) stands as a typical example of this class of materials, exhibiting a bulk lithium-ion conductivity of approximately 10^{-3} S/cm at room temperature. However,

*Corresponding author: +86 13705187680
e-mail: *huaianwwh@163.com* (W. Hu)
kongyazhou@hyit.edu.cn (Y. Kong)

the pronounced blocking effect of grain boundaries on lithium-ion transport results in a relatively low total conductivity, typically on the order of 10^{-5} S/cm, but LLTO maintains its considerable potential for practical applications [6]. Meanwhile, the practical application of LLTO is hindered by its poor chemical stability against lithium metal anodes and its high grain boundary resistance, which limits the total conductivity [7].

In recent years, research interest has shifted towards other perovskite systems structurally similar to LLTO, but with different chemical compositions, aiming to achieve superior overall performance. It was reported [8] that $Li_{0.25}La_{0.25}NbO_3$ (LLNO) is a promising candidate material among perovskite electrolytes. Zheng *et al.* [9] reported that the doping on the A-site of LLNO with alkaline earth ions can enhance the ionic conductivity of the perovskite solid electrolyte. Similarly, Kawakami *et al.* [10] found that doping the A-site of LLNO with elements of different ionic radii effectively modulates the conductivity of the perovskite lithium-ion conductor, providing important insights for designing high-performance solid electrolytes. Despite these advances, the intrinsic ionic conductivity of LLNO still requires further improvement to meet practical application demands. In the perovskite structure, the elemental species, valence state and coordination environment of the B-site cations directly determine the size, connectivity and migration energy barrier of the lithium-ion transport channels, making them key to tailoring ionic conductivity [11].

While conventional single-element doping strategies can yield certain improvements, their effectiveness is often limited and may introduce undesirable defects. In recent years, multi-element co-doping, also referred to as "high-entropy" doping, has gained increasing attention. As reported by Zeng *et al.* [12], the high-entropy mechanism can be leveraged to enhance ionic conductivity. This strategy involves introducing multiple elements with different sizes and valence states into a single crystallographic site, thereby inducing lattice distortion. It shows promise for significantly optimizing lithium-ion transport kinetics while maintaining the stability of the host crystal structure, potentially opening new pathways for reducing the activation energy for ion migration [13,14]. However, the systematic application of this multi-element co-doping strategy to the B-site of the LLNO system, along with in-depth investigation into the effects of varying doping concentrations on the material's structure, microstructure and electrical properties (particularly the coordinated regulation of ionic and electronic conductivity), remains an area requiring further exploration. In a related context, Fu *et al.* [15] reported a high-entropy garnet electrolyte, in which the introduction of four elements at the Zr-site resulted in excellent ionic conductivity, low activation energy and an extremely low electronic conductivity.

This study proposes high-entropy co-doping at the B-site of LLNO using five different cations, Ta^{5+} (69 pm), Hf^{4+} (79 pm), Zr^{4+} (80 pm), Ti^{4+} (68 pm), W^{6+} (62 pm), with ionic radii similar to that of Nb^{5+} (70 pm). This strategy aims to leverage the synergistic effects arising from the introduction of multiple elements to design entropy-stabilized ceramic materials and optimize their crystal structure and ion transport pathways. Using the conventional solid-state reaction method, we successfully synthesized a series of entropy-stabilized $Li_{0.25}La_{0.25}NbO_3$ ceramics with multi-element doping at the B-site. The effects of varying doping concentrations on the material's phase composition, microstructure, total ionic conductivity, electronic conductivity and activation energy for ion migration were systematically investigated. Ultimately, an optimized composition exhibiting both high ionic conductivity and low activation energy was identified. This work provides a new strategy and practical foundation for the design and development of high-performance perovskite-type solid electrolytes.

II. Experimental

2.1. Sample preparation

A series of ceramic samples, comprising an undoped $Li_{0.25}La_{0.25}NbO_3$ and three B-site co-doped compositions with varying stoichiometries, $(Li_{0.25}La_{0.25}Nb_{0.9}(Ta_{0.02}Hf_{0.02}Zr_{0.02}Ti_{0.02}W_{0.02})O_3$, $Li_{0.25}La_{0.25}Nb_{0.8}(Ta_{0.04}Hf_{0.04}Zr_{0.04}Ti_{0.04}W_{0.04})O_3$ and $Li_{0.25}La_{0.25}Nb_{0.7}(Ta_{0.06}Hf_{0.06}Zr_{0.06}Ti_{0.06}W_{0.06})O_3$), were synthesized via the solid-state reaction method. The undoped and co-doped samples were designated as LLNO, and LLNO-1, LLNO-2, LLNO-3, respectively.

Raw materials were weighed according to the stoichiometry of the samples LLNO, LLNO-1, LLNO-2 and LLNO-3. To compensate for lithium loss during calcination, Li_2CO_3 was added with 15 wt.% excess [16]. The starting materials included Li_2CO_3 (AR, 99.0%, Chengdu Kolon), La_2O_3 (99.9%, Aladdin), Nb_2O_5 (AR, 99.9%, Aladdin), Ta_2O_5 (99.5%, Aladdin), HfO_2 (99.9%, Shanghai Mogol), ZrO_2 (AR, 99.0%, Tianjin Yongda), TiO_2 (AR, 99.0%, Tianjin Yongda) and WO_3 (AR, 99.0%, Chengdu Kolon). The powder mixtures were homogenized via planetary ball milling at 250 rpm for 4 h using ethanol as a dispersing medium to ensure uniform particle distribution. The mixed powders were then pre-calcined at 900 °C for 12 h in air using a box furnace to decompose carbonate precursors. The calcined products were subsequently ground again in an agate mortar. The resulting powders were uniaxially pressed into pellets at 10 MPa using a hydraulic press. The pellets were sintered at 1100 °C for 12 h in air, followed by rapid air-quenching to room temperature to stabilize the phase. After sintering, the furnace was allowed to cool naturally from 1100 to 500 °C. The furnace door was then opened, and the samples were removed using tongs and allowed to cool to ambient temperature.

2.2. Characterization

Prior to all characterizations, the sintered pellets were polished using 400, 800 and 1200 grit sandpapers. The phase composition of the sintered pellets was determined by X-ray diffraction (XRD; Bruker D8 Advance) operated at 40 kV and 40 mA, with data collected over a 2θ range from 10° to 80°. Microstructural morphology and grain size were characterized using scanning electron microscopy (SEM; Hitachi S-3000N).

Ionic conductivity of the samples was measured with an HP 4192A impedance analyser over a frequency range of 5 Hz to 13 MHz. AC impedance spectra were recorded at temperatures ranging from 25 to 100 °C to determine the activation energy. Electronic conductivity was evaluated via the DC polarization method (ADCMT 6243R) by applying a constant 5 V bias for 6000 seconds at 25 °C. For both AC impedance measurements and DC polarization tests, electronically conductive graphite electrodes were applied by uniformly coating both surfaces of the electrolyte pellets with graphite.

The density of the ceramic samples was determined using the Archimedes principle (water displacement method). Prior to measurement, the samples were cleaned to remove surface contaminants. The dry mass (m_1) was measured using an analytical balance. The apparent mass in water (m_2) was obtained by suspending the sample in a wire basket and fully immersing the assembly into deionized water. The density was calculated using the following formula (where ρ_1 represents the density of water, taken as 1 g/cm^3):

$$\rho = \frac{m_1}{m_1 - m_2}\rho_1 \tag{1}$$

High-entropy oxides are defined as compounds comprising five or more principal elements occupying a shared cation sublattice, with each element constituting 5 to 35 at.% of the sublattice. This compositional complexity confers a configurational entropy (ΔS) exceeding 1.5R, distinguishing them from medium-entropy compounds ($R < \Delta S < 1.5R$) and low-entropy compounds ($\Delta S < R$). The configurational entropy (S_{config}) can be calculated using the following formula:

$$S_{config} = -R\sum_{i=1}^{n} x_i \ln x_i \tag{2}$$

where x_i is the mole fraction of the cationic species, and R is the universal gas constant [17]. Based on the calculated values, LLNO, with a configurational entropy of 0.867R, is classified as a low-entropy compound. LLNO-1 (1.191R) and LLNO-2 (1.412R) fall into the medium-entropy category, while LLNO-3 (1.595R) qualifies as a high-entropy compound.

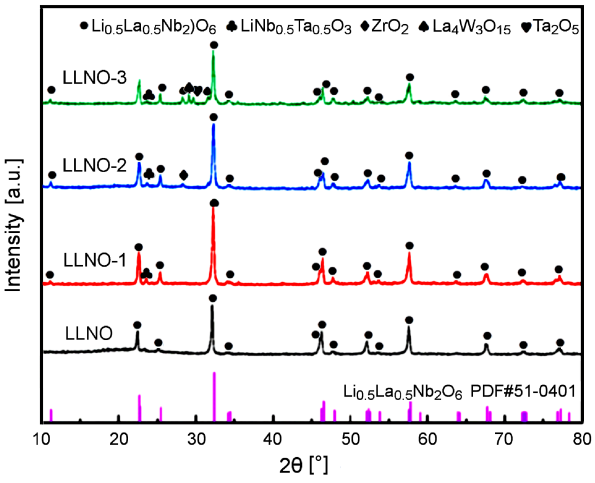

Figure 1. XRD patterns of the ceramic samples sintered at 1100 °C for 12 h

III. Results and discussion

3.1. Characterization of alumina powders

Figure 1 shows XRD patterns of the sintered LLNO, LLNO-1, LLNO-2 and LLNO-3 samples. The main diffraction peaks of all modified samples correspond well to the $Li_{0.5}La_{0.5}Nb_2O_6$ phase (PDF #51-0401), confirming the successful formation of a perovskite-type LLNO main phase. The LLNO ceramics has single phase composition. However, with increasing dopant concentration at the B-site in the prepared samples, several secondary phases were detected, including $LiNb_{0.5}Ta_{0.5}O_3$ (PDF #38-1252), ZrO_2 (PDF #72-1669), $La_4W_3O_{15}$ (PDF #49-0972) and Ta_2O_5 (PDF #54-0514). The formation of these secondary phases is primarily attributed to the co-doping of five elements at the B-site of LLNO, with minor contributions from lithium volatilization and incomplete high-temperature reactions. All four samples exhibit a strong, similar diffraction peak at approximately 33°, indicating the dominance of the corresponding crystal plane family and the high crystallinity of the main phase. A distinct peak near 24°, assigned to $LiNb_{0.5}Ta_{0.5}O_3$, is observed in the samples LLNO-1, LLNO-2 and LLNO-3. Similarly, both LLNO-2 and LLNO-3 ceramics exhibit clear peaks around 27.5° and a split peak near 32.5°, all identified as ZrO_2. For the LLNO-3 sample, additional distinct peaks appear near 28° and 29°, identified as $La_4W_3O_{15}$ and Ta_2O_5, respectively. The diffraction peaks in the XRD patterns of the of LLNO-1, LLNO-2 and LLNO-3 ceramics are shifted to higher angles by approximately 1° compared to the undoped LLNO. This shift towards higher angles suggests a decrease in interplanar spacing, likely induced by doping effects and the introduction of crystal defects. Overall, the increased concentration of the five co-doping elements successfully preserves the host crystal structure, albeit with the concomitant formation of secondary phases containing the dopants.

Figure 2 displays the fracture surface morphologies of the ceramic samples observed by scanning electron microscopy (SEM). The grain sizes of the LLNO, LLNO-1 and LLNO-3 ceramics range from 3 to 5 μm,

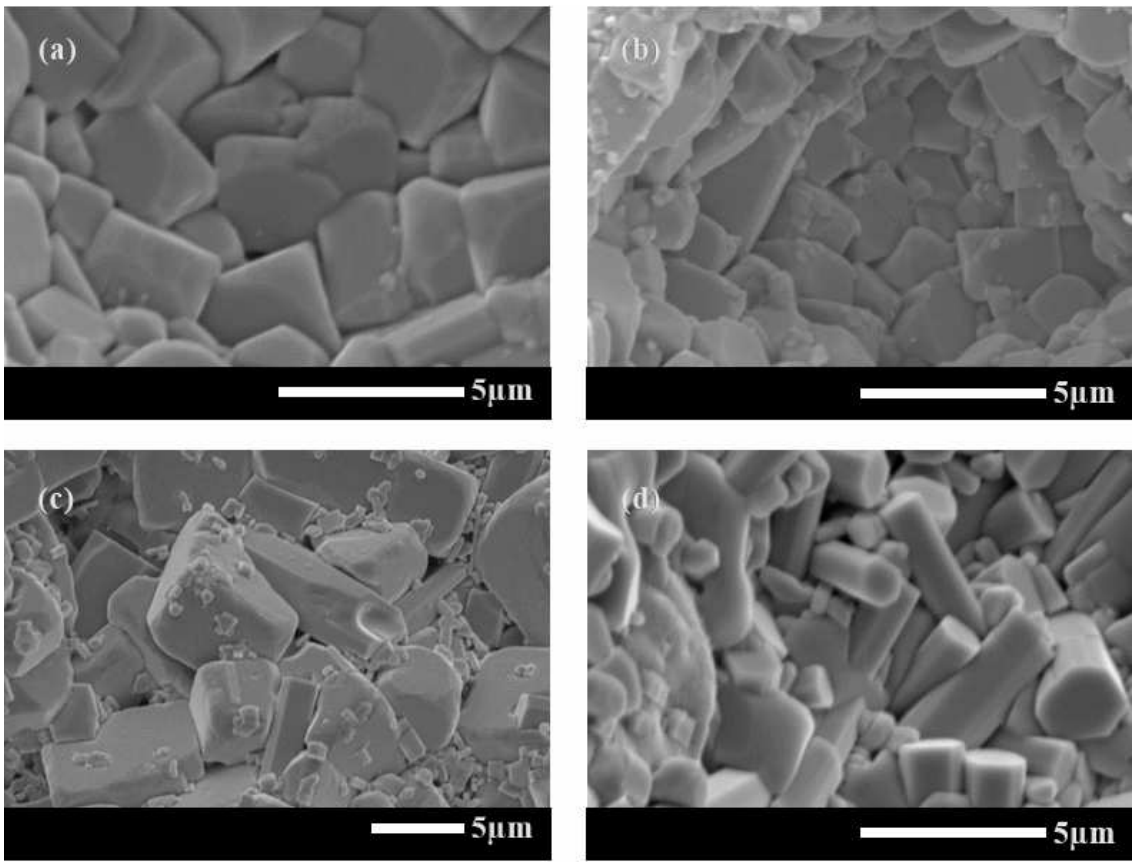

Figure 2. SEM images of the fracture surfaces of the ceramic samples: a) LLNO, b) LLNO-1, c) LLNO-2 and d) LLNO-3

while the LLNO-2 sample exhibits a larger grain size in the range of 8–13 μm. As shown in Table 1, the densities of these four samples, measured via the Archimedes principle (water displacement method), are nearly identical falling within the range of 4.74–4.82 g/cm^3. The relative densities of the four samples all fall within the range of 97 to 98 %TD. Among them, the LLNO-3 ceramics possesses the highest relative density, suggesting potentially optimal densification, which is beneficial for reducing grain boundary resistance and facilitating ion transport. The SEM images in Fig. 2 reveal highly compact grains with low number of large pores in all samples, indicating effective densification during the sintering process. The grains in the LLNO, LLNO-1 and LLNO-2 ceramics exhibit a quasi-tetragonal morphology, whereas those in the LLNO-3 ceramics display a rod-like structure, which may be attributed to the strong anisotropic growth inherent to the crystal structure of TiO_2, leading to the formation of rod-shaped crystals during sintering. Alternatively, this morphology could result from abnormal grain growth induced by excessive sintering. Furthermore, numerous fine particles are adhered to the grains in the structures of LLNO-1 and LLNO-2 ceramics, which may be attributed to the incomplete precursor reactions or the presence of secondary phases. In the SEM micrograph of the LLNO-3 sample, certain regions lack clearly defined grains, potentially due to the presence of amorphous phases or excessive sintering leading to the blurred grain boundaries and diminished crystallinity.

Figure 3 displays the AC impedance spectra of the prepared samples measured at various temperatures. Each Nyquist plot is characterized by a distinctive high-frequency semicircle. At room temperature (Fig. 3a), the resistance of the LLNO-1 sample (269.0 kΩ) is significantly higher than that of the undoped LLNO ceramics (159.7 kΩ). In contrast, the LLNO-2 and LLNO-3 ceramics exhibit substantially smaller semicircle diameters, corresponding to lower resistances of 71.77 kΩ and 49.66 kΩ, respectively. This trend indicates a continuous decrease in resistance with increasing concentration of the five-element co-dopants at the B-site. Although the sample dimensions are not identical, the differences are sufficiently minor to have a negligible impact on the impedance.

The resistance of all four ceramic samples consistently decreases with rising temperature (Fig. 3), demonstrating a significant thermal influence on their electrical behaviour. Thus, the resistance of the LLNO-1 sample decreases from 261.8 to 37.39 kΩ, while the resistances of the LLNO, LLNO-2 and LLNO-3 ceramics all drop from approximately 100 kΩ to around 40 kΩ with increasing temperature (Figs. 3b-e). Furthermore, as temperature increases, the low-frequency linear regions of the spectra for all samples gradually converge. As shown in Table 1, the total ionic conductivity in-

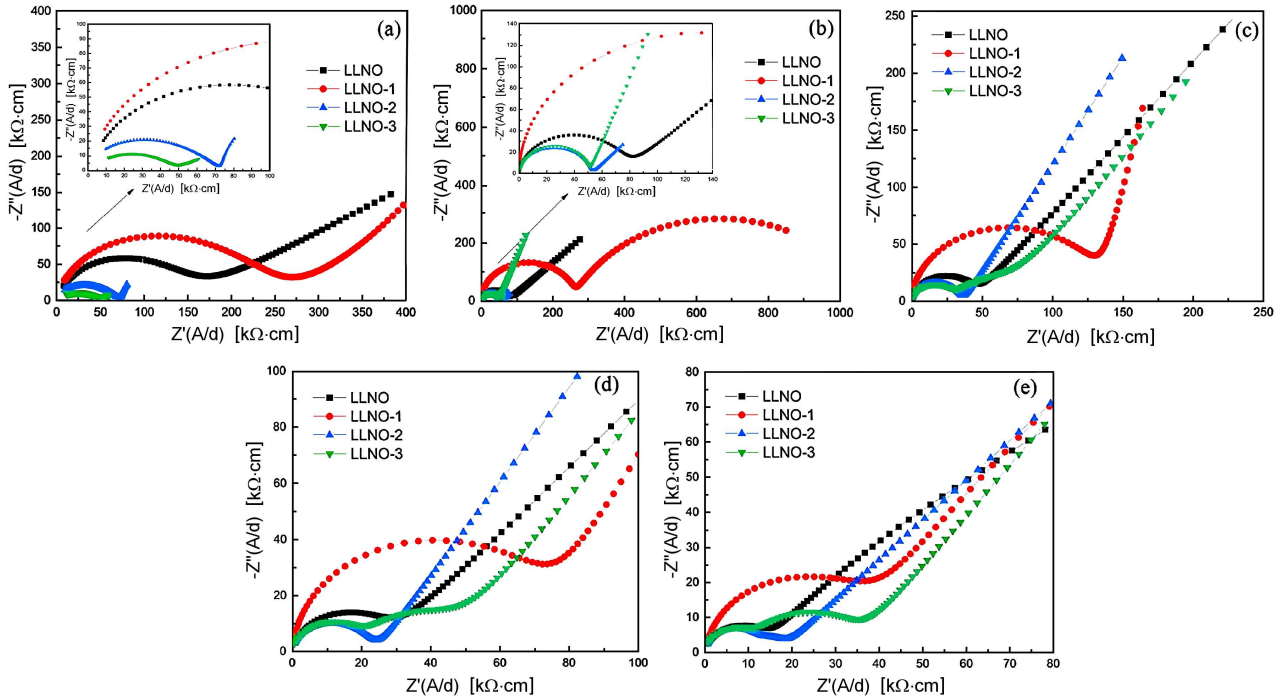

Figure 3. Nyquist plots of the ceramic samples measured at different temperatures: a) 25, b) 40, c) 60, d) 80 and e) 100 °C

Table 1. Density, relative density, ionic conductivity, electronic conductivity and activation energy of the ceramic samples

Sample	Density [g/cm^3]	Relative density [%TD]	$\sigma_{25\,°C\text{–total}}$ [S/cm]	$\sigma_{25\,°C\text{–ele}}$ [S/cm]	E_a [eV]
LLNO	4.765	97.37%	1.17×10^{-6}	2.97×10^{-8}	0.315
LLNO-1	4.743	96.86%	1.11×10^{-6}	4.72×10^{-8}	0.289
LLNO-2	4.756	97.02%	4.68×10^{-6}	5.30×10^{-8}	0.206
LLNO-3	4.824	98.67%	6.44×10^{-6}	1.28×10^{-7}	0.218

creases remarkably with increasing dopant concentration at the B-site, showing an approximately sixfold enhancement (from 1.17×10^{-6} S/cm to 6.44×10^{-6} S/cm). A direct correlation exists between increased co-doping concentration and enhanced conductivity. Although the LLNO-3 ceramics emerges as the definitive optimal choice when prioritizing conductive properties, its conductivity is still far below the requirements for practical applications (> 10^{-4} S/cm).

Figure 4 displays the Arrhenius plots of $\log(\sigma T)$ versus $1000/T$ for all samples. The fitted curves for all compositions demonstrate approximately linear relationships. The downward trend of the curves confirms the characteristic increase of conductivity with temperature, consistent with thermally activated ion transport. The LLNO-2 and LLNO-3 samples exhibit steeper slopes than the LLNO and LLNO-1, indicating lower activation energies for the higher-doped compositions. As summarized in Table 1, the activation energy, E_a (the energy barrier for ion migration), decreases significantly from 0.315 eV for the undoped LLNO to 0.218 eV for the highly doped LLNO-3 sample. This reduction provides compelling evidence that the modifications in the LLNO-2 and LLNO-3 ceramics effectively create more

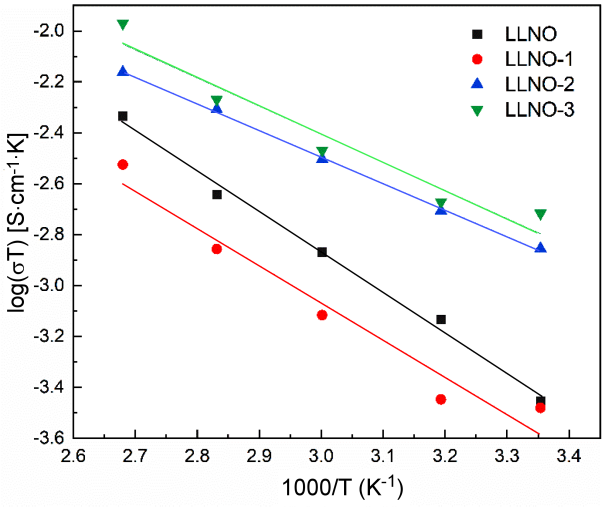

Figure 4. The Arrhenius plots of the ceramic samples

energetically favourable pathways, thereby facilitating lithium ion hopping.

The electronic conductivity of the ceramic samples was measured using the ion-blocking DC polarization method with graphite electrodes coated on both sample

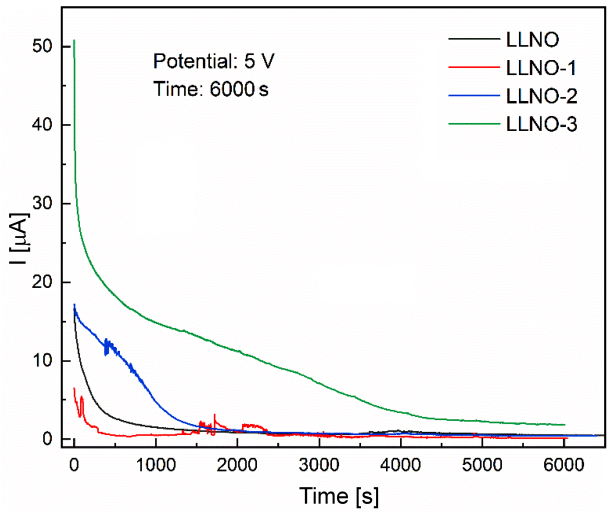

Figure 5. DC polarization curves of the prepared ceramic samples

surfaces. The DC polarization results are presented in Fig. 5. For the LLNO, LLNO-1 and LLNO-2 samples, the current reached a steady state after approximately 2000 s, indicating complete ion blocking. While slight current fluctuations were observed during the testing the LLNO-1 ceramics, the overall signal remained stable. In contrast, the LLNO-3 sample required about 5000 s to stabilize. The observed gradual current decay in polarization curve could be due to the surface passivation, reactant consumption, or decreased electrode activity. At 25 °C, the electronic conductivities were measured to be 2.97×10^{-8} S/cm, 4.72×10^{-8} S/cm, 5.30×10^{-8} S/cm and 1.28×10^{-7} S/cm for the LLNO, LLNO-1, LLNO-2 and LLNO-3 ceramics, respectively. These values are approximately 1–2 order of magnitude lower than the corresponding total conductivities. Although the electronic conductivity remains low, its increasing trend warrants attention. This suggests that while the doping strategy effectively optimizes ion transport pathways, it may simultaneously introduce certain defects (such as oxygen vacancies or multivalent ions) that could enhance electronic leakage.

IV. Conclusions

A simple solid-state reaction method was used to synthesized undoped $Li_{0.25}La_{0.25}NbO_3$ (LLNO) and three entropy-stabilized ceramics, i.e. $Li_{0.25}La_{0.25}Nb_{1-x}M_xO_3$ where x = 0.02, 0.04 and 0.06 (LLNO-1, LLNO-2 and LLNO-3) and M denotes five cations (Ta^{5+}, Hf^{4+}, Zr^{4+}, Ti^{4+}, W^{6+}) with equimolar content. The structures and electrical conductivities of these four ceramic samples were systematically investigated. Experimental results indicate that all samples possess a perovskite structure, but the presence of secondary phases was observed in $Li_{0.25}La_{0.25}Nb_{1-x}M_xO_3$ ceramics. The LLNO-3 ceramics shows the highest conductivity of all the samples, reaching 6.44×10^{-6} S/cm, electronic conductivity of 1.28×10^{-7} S/cm and activation energy of 0.218 eV. An approximate sixfold enhancement (from 1.17×10^{-6} S/cm to 6.44×10^{-6} S/cm) in conductivity was observed in comparison to the undoped LLNO sample. These results demonstrate that high-entropy doping at the B-site can effectively improve the conductivity of LLNO, but excessive high-entropy doping may adversely affect the overall electrical properties of the material.

Acknowledgement: This work was supported by the Research Start-up Fund of Huaiyin Institute of Technology (Z301B20574), the fund of National & Local Joint Engineering Research Center for Mineral Salt Deep Utilization (SF202206), Natural Science Foundation of the Higher Education Institutions of Jiangsu Province (23KJB450001), Foundation of Key Laboratory for Palygorskite Science and Applied Technology of Jiangsu Province (HPZ202201).

References

1. J. Janek, W.G. Zeier, "A solid future for battery development", *Nat. Energy*, **1** (2016) 16141.
2. A. Manthiram, X. Yu, S. Wang, "Lithium battery chemistries enabled by solid-state electrolytes", *Nat. Rev. Mater.*, **2** (2017) 16103.
3. D. Shieh, S.F. Wang, P.W. Chi, Y.F. Hsu, M.K. Wu, "Preparation of all solid-state electrolyte lithium ion batteries by multi-layer co-fired process", *Process. Appl. Ceram.*, **19** [1] (2025) 94–107.
4. P. Knauth, "Inorganic solid Li ion conductors: An overview", *Solid State Ionics*, **180** [14-16] (2009) 911–916.
5. S. Stramare, V. Thangadurai, W. Weppner, "Lithium lanthanum titanates: A review", *Chem. Mater.*, **15** [21] (2003) 3974–3990.
6. Y. Inaguma, C. Liquan, M. Itoh, T. Nakamura, T. Katsumata, Y. Morii, "High ionic conductivity in lithium lanthanum titanate", *Solid State Commun.*, **86** [10] (1993) 689–693.
7. Y. Maruyama, M. Nagao, S. Watauchi, I. Tanaka, "Synthesis and ionic conductivity of $Li_xLa_{(1-x)/3}Nb_{1-y}Ta_yO_3$ solid solutions", *J. Ceram. Soc. Jpn.*, **128** [10] (2020) 761–765.
8. K. Kawahara, R. Ishikawa, K. Nakayama, T. Higashi, T. Kimura, Y.H. Ikuhara, N. Shibata, Y. Ikuhara, "Fast Li-ion conduction at grain boundaries in (La,Li)NbO_3 polycrystals", *J. Power Sources*, **441** (2019) 227187.
9. J.Q. Zheng, Y.F. Li, R. Yang, G. Li, X.K. Ding, "Lithium ion conductivity in the solid electrolytes $(Li_{0.25}La_{0.25})_{1-x}M_{0.5x}NbO_3$ (M = Sr, Ba, Ca, x = 0.125) with perovskite-type structure", *Ceram. Int.*, **43** [2] (2017) 1716–1721.
10. Y. Kawakami, M. Fukuda, H. Ikuta, M. Wakihara, "Ionic conduction of lithium for perovskite type compounds, $(Li_{0.05}La_{0.317})_{1-x}Sr_{0.5x}NbO_3$, $(Li_{0.1}La_{0.3})_{1-x}Sr_{0.5x}NbO_3$ and $(Li_{0.25}La_{0.25})_{1-x}M_{0.5x}$ NbO_3 (M = Ca and Sr)", *Solid State Ionics*, **110** [3-4] (1998) 187–192.
11. Y. Deng, C. Eames, J.N. Chotard, F. Lalere, V. Seznec, S. Emge, O. Pecher, P. Grey, C. Masquelier, M. Witter, M. Islam, "Structural and mechanistic insights into fast lithium-ion conduction in $Li_{4-x}Ge_{1-x}P_xS_4$ solid electrolytes", *J. Am. Chem. Soc.*, **137** [28] (2015) 9136–9145.

12. Y. Zeng, B. Ouyang, J. Liu, Y.W. Byeon, Z. Cai, L.J. Miara, Y. Wang, G. Ceder, "High-entropy mechanism to boost ionic conductivity", *Science*, **378** [6626] (2022) 1320–1324.
13. C.M. Rost, E. Sachet, T. Borman, A. Moballegh, E.C. Dickey, D. Hou, J.L. Jones, S. Curtarolo, J.P. Maria, "Entropy-stabilized oxides", *Nat. Commun.*, **6** (2015) 8485.
14. S.C. Kim, J. Wang, R. Xu, O. Kahvecioglu, Y. Tian, Y. Li, Y. Huang, Y. Li, J. S. Kim, G. Ceder, "High-entropy electrolytes for practical lithium metal batteries", *Nat. Energy*, **8** (2023) 814–826.
15. Z. Fu, J. Ferguson, "Processing and characterization of an $Li_7La_3Zr_{0.5}Nb_{0.5}Ta_{0.5}Hf_{0.5}O_{12}$ high-entropy Li-garnet electrolyte", *J. Am. Ceram. Soc.*, **105** [10] (2022) 6175–6183.
16. S. Hu, S. Zhang, C. Cai, Z. Wang, J. Chang, Y. Kong, H. Wang, K. Zhang, G. Hu, W. Hu, H. Sun, J. Wang, J. Zhang, K. Hong, "Effect of excess lithium on the electrical properties of $Li_{0.25}La_{0.25}NbO_3$ ceramics", *Optoelectron. Adv. Mater. Rapid Commun.*, **18** [9-10] (2024) 490–494.
17. C. Wang, L. Zhang, H. Xie, G. Pastel, J. Dai, Y. Gong, B. Liu, E.D. Wachsman, L. Hu, "Mixed ionic-electronic conductor enabled effective cathode-electrolyte interface in all solid state batteries", *Nano Energy*, **50** (2018) 393–400.